CHICAGO JOURNALS

MIRSI, A Mid-Infrared Spectrometer and Imager: Performance Results from the IRTF

Marc Kassis[1]

Keck Observatory 65-1120 Mamalahoa Hwy, Kamuela, HI; mkassis@keck.hawaii.edu

Joseph D. Adams[1]

Cornell University Department of Astronomy 206 Space Sciences Bldg., Ithaca, NY; jdadams@astro.cornell.edu

Joseph L. Hora[1] and Lynne K. Deutsch[2]

Harvard-Smithsonian Center for Astrophysics 60 Garden Street, MS-65, Cambridge, MA; jhora@cfa.havard.edu

and

Eric V. Tollestrup

NASA Infrared Telescope Facility 640 N. Aohoku Pl. Hilo, HI; tolles@ifa.hawaii.edu

ABSTRACT. The Mid-Infrared Spectrometer and Imager (MIRSI) is a mid-infrared camera system built at Boston University for ground-based observing. MIRSI offers complete spectral coverage over the atmospheric windows at 8–14 and 18–26 μm for both imaging (discrete filters and a circular variable filter) and spectroscopy (in the 10 and 20 μm windows with resolutions of $\lambda/\Delta\lambda = 200$ and 100, respectively). The optical design was optimized for use at NASA's Infrared Telescope Facility (IRTF). MIRSI utilizes a 320×240 pixel detector array with a plate scale of $0.27''$ pixel^{-1}, covering a field-of-view of $86'' \times 63''$ at the IRTF. MIRSI's optics provide diffraction-limited spatial resolution, and the instrument achieves $1\,\sigma$ detection limits of 4 and 236 mJy at 10 and 21 μm, respectively, in 60 s of on-source integration time.

Online material: color figure

1. INTRODUCTION

The Mid-Infrared Spectrometer and Imager (MIRSI; Deutsch et al. 2003) was designed for the study of a number of astrophysical phenomena that require ground-based thermal infrared observations. The motivation to build MIRSI grew out of our experience with the Mid-Infrared Array Camera (MIRAC; Hoffmann et al. 1993, 1998), which we had used on the Infrared Telescope Facility (IRTF) and telescopes in Arizona. A new generation of larger format mid-IR arrays had become available that enabled much larger field sizes and also had relatively low dark current that would allow background-limited low-resolution spectroscopy. MIRSI's combined spectroscopic and imaging capabilities make it possible to correlate the spatial and spectral features observed in astrophysical sources and thereby reveal key physical and chemical processes. MIRSI

was designed to enable ground-based observations at high spatial resolution with background-limited sensitivity. The system has the capability to acquire both broadband and narrowband images, and low-resolution grism spectra within the two atmospheric windows at 8–14 and 17–26 μm. MIRSI was designed to be mounted at the Cassegrain focus of the IRTF. A summary of the design specifications is given in Table 1.

MIRSI is based on a reflective, off-axis optical system. All optics, filters, grisms, and the detector are mounted on a 4.7 K work surface housed in a cryogenic (LN$_2$ and LHe) dewar, which was developed under our direction at Infrared Laboratories (Tucson, AZ). The camera control electronics hardware and software were obtained from Astronomical Research Cameras, Inc. (ARC Gen II; San Diego State University, San Diego, CA). We adapted the control system software to accommodate infrared array control and incorporated filter wheel motor control, temperature monitoring, image display, and telescope control routines that are required for mid-infrared observing. A more detailed description of the optical system, dewar, electronics, computer control, system integration, and the modifications made to both hardware and software can be found in Deutsch et al. (2003).

---

[1] Visiting Astronomer at the Infrared Telescope Facility, which is operated by the University of Hawaii under a cooperative agreement with the National Aeronautics and Space Administration.

[2] Deceased. Lynne K. Deutsch was the Principal Investigator of the MIRSI instrument.

1271

TABLE 1

SUMMARY OF MIRSI SPECIFICATIONS AT THE IRTF

Operating Spectral Range	8–14 & 17–26 μm
Number of pixels	320×240
Pixel size	50 μm
Dewar type	Cryogenic (4.7 K)
Pixel Scale	0.27 arcsec/pixel
Field of View	86×63 arcsec
Point-source sensitivity (10 μm)	4 mJy in 60 seconds integration
Spectroscopic Resolution	100 or 200
Grism Dispersion (10 μm)	0.01866 μm pixel^{-1}
Grism Dispersion (20 μm)	0.0325 μm pixel^{-1}

After MIRSI was first used by the instrument team at the IRTF in 2002, the system has remained on Mauna Kea and the IRTF has operated MIRSI as a collaborative PI/facility instrument. The staff at the IRTF has supported observers, performed maintenance and improvements to the electronics and software, replaced filters and windows, and handled the routine cryogenic operations. Over the past four years, observers at the IRTF have been awarded use of MIRSI on ~35 nights a semester to acquire imaging and spectroscopic observations of such targets as young stellar objects (e.g., Campbell et al. 2008; Smith et al. 2005), star formation regions, molecular clouds (Kassis et al. 2006), planetary and protoplanetary nebulae, starburst galaxies, and solar system objects such as planets (Sanchez-Lavega et al. 2008; Baines et al. 2007), asteroids (Mueller et al. 2007; Tedesco et al. 2005), and comets (Harker et al. 2004; Fernandez et al. 2004).

In the sections to follow, we present performance and calibration results based on science and engineering data acquired at the IRTF.

2. MIRSI OPTICAL DESIGN

In order to understand how to calibrate the observations obtained with MIRSI, it is helpful to know the details of the optical design. The instrument was built to support the optical layout shown in Figure 1. The mirror specifications are given in Table 2. The all-reflective design using aluminum mirrors allowed the system to be aligned at optical wavelengths at room temperature, and provides high throughput. The optics were designed for diffraction-limited imaging on the IRTF over the 8–26 μm range and over a wide field of view (FOV), as well as for properly sizing the pupil to be compatible with using the CVF and grisms. The $f/37$ beam from the telescope (coming from the top of Fig. 1) enters the dewar through a KRS-5 window. The telescope focus is at the position of the aperture or slits that are machined into a wheel at the entrance to the dewar. The aperture can be blocked with a cold shutter in order to conserve helium when MIRSI is not being actively used. A fold mirror (M1) directs the light into the collimating mirror (M2) and then through the filters and pupil stop. The pupil stop is located between the filter wheels and is approximately 5 mm in diameter.
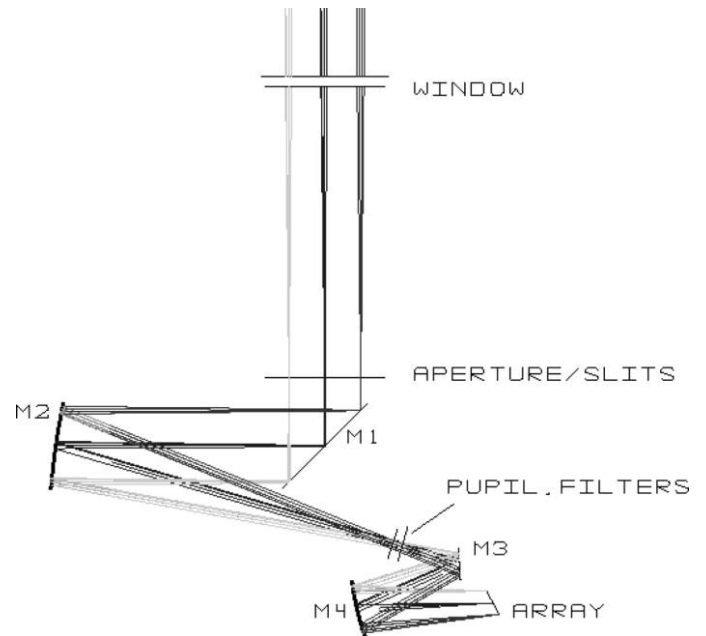

FIG. 1.—Ray tracing of the MIRSI optical design. The light from the telescope comes from the top of the image and enters the dewar through the KRS-5 window. A fold mirror (M1) directs the light into the collimating mirror (M2) and then through the filters and pupil stop. The camera mirrors M3 and M4 then reimage the focal plane onto the detector. See the electronic edition of the PASP for a color version of this figure.

The filter wheels are enclosed in a box that, along with other baffles, ensures that any light must pass through the filters and pupil before being reflected from the camera mirrors M3 and M4 that reimage the focal plane onto the detector. The use of cryogenic stepper motors to operate the wheels eliminates the need for mechanical feedthrough and ensures that light leaks into the dewar are minimized.

Because of the off-axis design, the optical axis is not perpendicular to the detector surface in the plane shown in Figure 1. This leads to a difference in scale between the long and short dimensions of the array, as discussed in § 4.

3. ARRAY PERFORMANCE

MIRSI's detector is a "science grade" Si:As blocked impurity band (BIB) array (320×240 pixels) developed by Raytheon (Goleta, CA; e.g., Estrada et al. 1998). The array is connected to

TABLE 2

MIRSI MIRROR PARAMETERS

Mirror	Conic	Radius (mm)	Off-axis (mm)	Comments
M1	0	...	0	Folding flat
M2	−1	350	45.009	Collimator
M3	−245.6902	298.5164	9.500	Camera mirror 1
M4	−0.4757	113.8440	30.513	Camera mirror 2

a CMOS readout integrated circuit through indium bump bonds and mounted to a leadless chip carrier. MIRSI is configured to read out the detector in 16-channel mode. Well depths of $3 \times 10^7 \ e^-$ or $1 \times 10^7 \ e^-$ can be chosen. We chose to set the well depth to $3 \times 10^7 \ e^-$ in order to operate closer to background-limited performance and minimize the effects of excess electronics noise (see Deutsch et al. 2003). The bias across the detectors is 2.3 V, which was determined, using lab measurements of the lab ambient thermal background, to be the bias that provides the best signal-to-noise ratio. Table 3 provides a summary of the nominal detector characteristics. The gain reported in Table 3 is an estimate based on measurements of standard stars and assumptions of the optical transmissions and detector QE.

3.1. Linearity

To determine the linearity of the detector, we acquired images of the ambient thermal background in the lab at 4.9 μm using frame times from ~4 to ~70 ms. We determined the mean of the central 21×21 pixels in each image, and then performed a linear fit to the mean as a function of time (see Fig. 2). We define the array to be operating in a nonlinear regime when the departure from linearity is greater than one percent. This occurred at frame times longer than 52 ms. Thus, the nonlinear regime occurs when the mean flux is greater than ~45,000 analog to digital units (ADU). The zero level is approximately 10,000 ADU, giving a linear range of 35,000 ADU (~70% full well). Table 4 shows typical frame times selected by observers to operate the detectors in the background noise limited flux range but low enough to avoid image saturation. The flux of the object + sky must be lower than the maximum linear value. In most cases, the brightest objects one will observe will be the IR standard stars, which can be a few hundred ADU in the 10% bandwidth filters. Therefore the sky and telescope background provide the dominant flux and determine
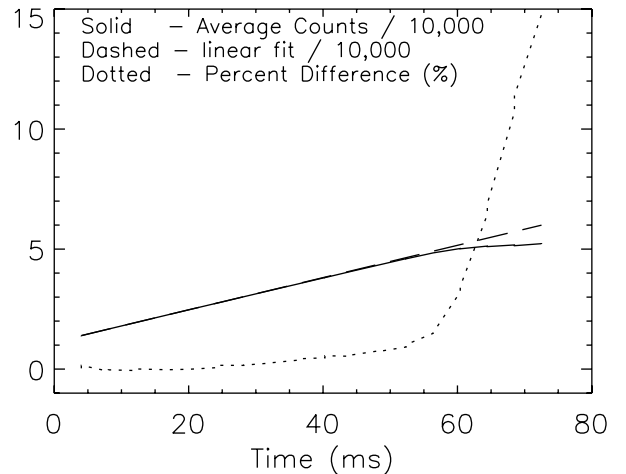

Fig. 2.—Linearity of the MIRSI detector response. The solid line is the observed signal as a function of frame time, and the dashed line is a linear fit to the data from 0–40 ms. The percent error is plotted as the dotted line. The fit and the observed counts are reduced by a factor of 10,000.

which frame time is chosen. The sky and telescope background will change depending on temperature and sky conditions, so the observer must monitor the background flux and adjust the frame time as necessary.

3.2. Responsivity and Flat-Fielding

The responsivity of the detector in MIRSI was determined using calibration flats acquired on the dome and sky at the IRTF on 2004 27–29 December. For the dome observations, the telescope was pointed at a section of the dome specifically painted for calibrations. For the sky observations, the dome was rotated without moving the telescope so that the telescope looked out the dome slit. This avoids any changes in illumination due to flexure of the telescope or instrument. For both dome and sky observations, 11 images were acquired and then median-combined. To create the gain map (Fig. 3), we differenced

TABLE 3

SUMMARY OF MIRSI SI:AS BIB DETECTOR ARRAY CHARACTERISTICS

Wavelength Range	2–26 μm
Number of pixels	320×240
Pixel pitch	50 μm
Material	Si:As
Technology	IBC
Operating temperature	5.5 K
Peak quantum efficiency	>40%
Frame Rates	$\geq$250 Hz
Number of outputs	16
Well depth	$3 \times 10^7 \ e^-$
Read noise	<2800 e^-
Nonlinearity	$\leq$10%
Operability	99%
Power dissipation	~140 mW
e^-/ADU	800

TABLE 4

TYPICAL FRAME TIMES USED

Filter (μm)	Frame time (ms)
2.2	32
4.9	36
7.8	36
8.7	32
9.8	32
N-band	20
11.6	64
12.282	32
12.5	56
18.5	80
20.9	4
24.5	24
10 μm Grism	500

the dome and sky images and divided by the mean. One would therefore divide their data by this image to correct for the gain variations across the detector. In the gain map, the observed pixel-to-pixel variations are due to different channel amplifier gains, system gains, optical throughput, detector response, and array pattern noise (see § 5).

A histogram of the array responsivity determined from the 11.6 μm gain map is shown in Figure 3, and the mean, median, standard deviation, minimum, and maximum responsivity are presented in Figure 4. The responsivity measurements confirm the manufacturer's specifications that the detector has more than 99% operable pixels. We exclude the last row of 320 pixels because they behave differently due to the detector readout scheme (Deutsch et al. 2003). There is a low gain wing in the responsivity, which is mostly due to field vignetting in the corners of the array.

At two standard deviations from the responsivity mean, the array is flat to within 15%. These pixel-to-pixel variations are significant, and so we recommend that a gain correction such as the one shown in Figure 3 be applied to MIRSI data. We found that gain maps from night to night show variations on the order of 0.3%. Thus, depending on the desired photometric precision, it may not be necessary to acquire flats for each filter on every observing night. However, the collimation of the instrument and telescope might affect the throughput across the field, so gain maps should be acquired at least once for each observing run and when different rotation angles are used.

3.3. Dark Current

To measure the array dark current, images at different exposure times were taken with the aperture wheel positioned between slit positions, the LN$_2$ baffle closed, and a cold aluminum blank located at the pupil in the filter wheel to mini-
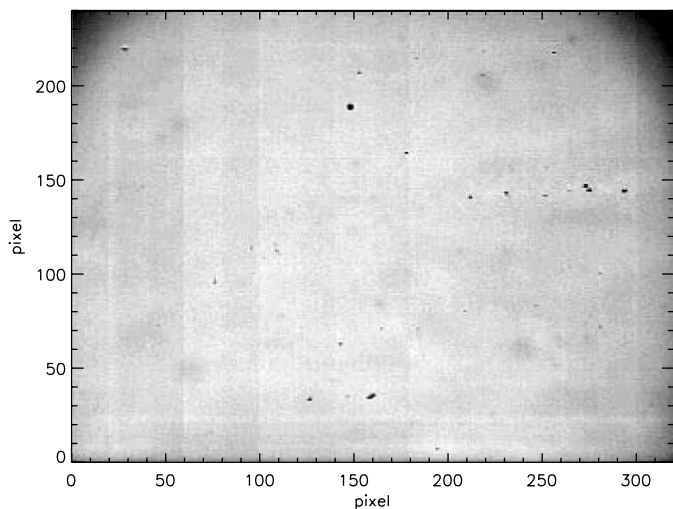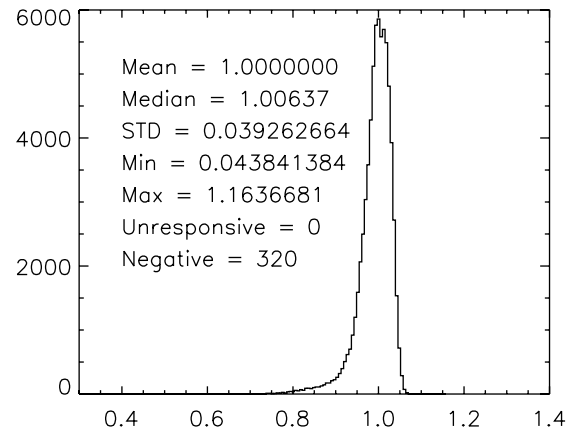
FIG. 4.—Histogram of the gain values at 11.6 μm. The mean, median, standard deviation, minimum maximum, number of unresponsive pixels, and the number of nonlinear pixels of the distribution is provided in the upper left. The array is flat to within 15% (2 σ variation).

mize the flux level on the array. These images were taken in the laboratory in 2002 September with a detector operating temperature of 5.5 K and frame times from 4 ms to 40 s. We performed a linear fit to the data to determine an average dark current of $64,000$ e^- s^{-1}. Although this is larger than the manufacturer specification of 100 e^- s^{-1}, it is still sufficiently low and will add negligible noise in standard chop and nod observing modes with the background levels experienced at the IRTF.

3.4. Bad Pixels

To create a bad pixel map, we subdivided the gain maps into 10×10 pixel images. The mean and standard deviation in each subimage were calculated after excluding the 10 highest and 10 lowest valued pixels. Pixels with gain values more than 10 standard deviations from the mean were identified as bad pixels. Using this method, vignetted pixels were not flagged as bad pixels.

A composite bad pixel map (see Fig. 5) contains 83 pixels that are identified as bad (excluding readout effects in the last row). With this number of bad pixels, the detector in MIRSI is more than 99% operable and is consistent with the operability specified by the manufacturer (Raytheon 1999). The 83 bad pixels are predominantly located in one quadrant of the array. By dithering between images, the effects due to bad pixels are minimized.

4. PLATE SCALE AND FOV

The plate scale and distortion were determined from observations of a standard star that was offset using the telescope to a grid of positions on the array. This method was used because there is no good field of bright mid-infrared sources with precise astrometric positions distributed uniformly over a 1′ field. It does lead to the result being dependent on the accuracy of the IRTF

FIG. 3.—MIRSI gain map at 11.6 μm. Darker areas have lower system gain. Values range from 0.8 to 1.05, normalized to a mean of 1.
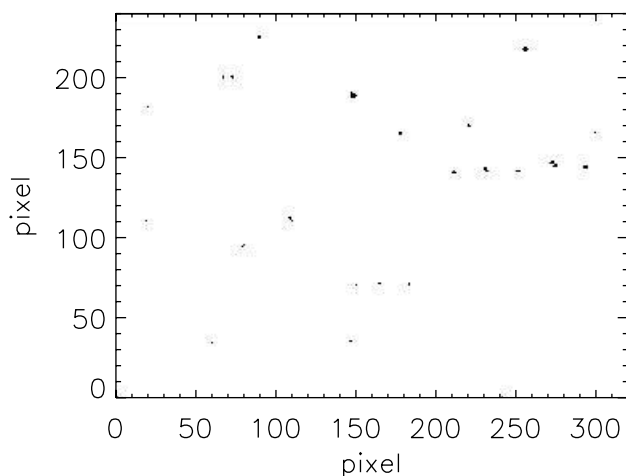
FIG. 5.—MIRSI bad pixel map. The dark areas (pixels with values of 0) identify bad pixels on the array.

pointing calibration. However, the offsets included many repetitions of the center position to act as a reference for removing any telescope drift during the period of the measurement.

The observations were performed on the standard star μ UMa using a chop throw of 30″ N–S and nod of 40″. MIRSI was in its nominal orientation at a rotation of 0°, which maps declination along the short axis and right ascension along the long axis of the detector. All four beams were kept on the array, and offsets were performed to step the primary beam around one quadrant of the array in 5″ steps. The chop and nod distances were adjusted so that the off beams were positioned on the other three quadrants of the detector. Seven offsets were obtained between each observation of the reference position. A drift rate of approximately 1″ min^{-1} was measured in right ascension, which was used to correct the measured offset positions. No significant drift in declination was observed during the observations. Because nods use the same method to move the telescope as dithering, the nod positions should be just as accurate. The chop throw is set using separate electronics that controls the throw of the IRTF secondary mirror, so the chop setting was not assumed accurate. Instead, the scale in the chop throw was estimated based on subsets of the dithered offsets that were in declination only. After the scale and distortion were fit as described below, the result for the declination scale were used to refine the estimate of the chop throw and the data was refit. We iterated a number of times to refine the chop throw distance until it converged to 28.88″.

The pixel scale and distortion can be reasonably fit by a linear scale of 0.26894″ pixel^{-1} along the long axis and 0.26355″ pixel^{-1} along the short axis, giving a FOV of approximately 86″ × 63″. A second-order polynomial fit gives slightly lower residuals and differs from the linear fit by less than 1/3 pixel (0.08″) at the extreme corners of the array. Within a radius of 30″ from the center, the difference between the linear and polyno-

mial fit is 0.1 pixel or less. The appendix gives the database file produced by the IRAF[3] function `geomap` using a second-order polynomial fit to the offset data positions.

5. NOISE ARTIFACTS

There are common noise artifacts that are present in MIRSI data in both imaging and spectroscopic modes. One noise artifact is present when the light from a source is sufficiently brighter than the background flux. The signal level drops in pixels located in the same readout channel and above the bright source (see Fig. 6). In addition, a level drop is noticed in pixels in other readout channels along the same row as the bright source. Figure 6 also shows that, for bright sources, ghosting at the <1% level is detected.

The level drop problem and a solution is well documented by Sako et al. (2003) who identify the cause as transient variations of the source followers in the array readout circuit. The level shift problem is often seen when imaging or acquiring spectra of standards that are typically brighter than most sources. To quantify how the level shift affects a flux measurement from a bright source, we measured the average background flux around a standard star in a chop-nod image set. Two background areas were sampled and only one included a portion of the background where a level shift was present. The difference between measurements of the background and a background that included a level shift was 0.5%. Typically, observers chop and nod along the rows and columns of the array as this is the default setup at the IRTF. However, it is possible to adjust the direction of the telescope chop and nod throws such that the target always lands in a different readout channel, thereby minimizing the level drop effects when observing bright sources.

There is also a pattern noise that when first seen appears to be random offsets in the flux level from row to row. Within a row, however, the pixel-to-pixel variations are repeated every 20 pixels or within every readout channel. Thus, the pattern noise is found to be common to all readout channels (see Fig. 7), but the pattern changes from frame to frame.

We have developed routines to reduce the pattern noise in imaging and spectroscopy data, and the routines are used following the combination of chop-nod data sets and flat-fielding. One method for removing the pattern noise is to median filter the 16 readout channels to determine the common pattern. The median pattern is then subtracted from each of the 16 readout channels to reduce the noise. For this method to work, we assume that the sky flux is uniform across the array. This method works well for the most common type of imaging data where a single compact source is chopped and nodded on the array. The median statistic rejects the few locations where the source is on
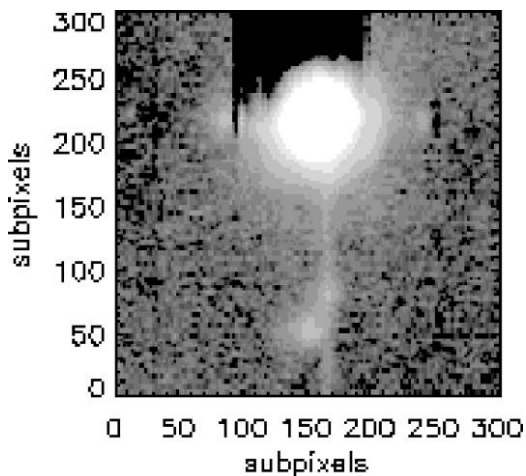
FIG. 6.—Image of α Tau, obtained with MIRSI, that exhibits two image artifacts. The channel darkens above the bright point source (level drop effect). For bright point sources, there are small ghosts that are visible in this image at subpixel 150, 50.

the image and an accurate estimate of the common pattern noise can be constructed and subtracted from the image. In some regions, such as the Orion Nebula, there is a diffuse emission at 10 μm that fills the FOV. Although this means we cannot assume that the sky flux is uniform, the images in Figure 7 demonstrate the benefit of median filtering. There is more structure visible in the Trapezium region after median filtering the pattern noise.

To quantify the benefits of median filtering the pattern noise, we measured the background noise in the μ UMa image set used to determine the pixel scale and FOV in the section above. A total of 146 images each with a total exposure time of 0.9672 s were used. We co-added the images in sets with an increasing number of exposures in each set and determined the noise as a function of exposure time. Figure 8 shows how the noise in the background decreases with time for images with and without the pattern noise median filtered. By median filtering the data across the channels, the noise is reduced by a factor of 3 (see Fig. 8).

For spectroscopy, we use a different approach because the sky flux is not uniform across the array. In 10 μm spectra obtained with MIRSI, the N-Band filter is used as a blocking filter, and because the filter's long wavelength cutoff is at 13.3 μm, it prevents light from exposing the last readout channel. Therefore, the last readout channel may serve as a template for the pattern noise, and we subtract the 16th readout channel from the other 15 channels to suppress the pattern noise.

6. IMAGE PROCESSING

The instrument data are stored as 2D FITS files that contain one image followed by 1 or 3 image extensions (the off-source chop and nod images are stored as the extensions). The FITS
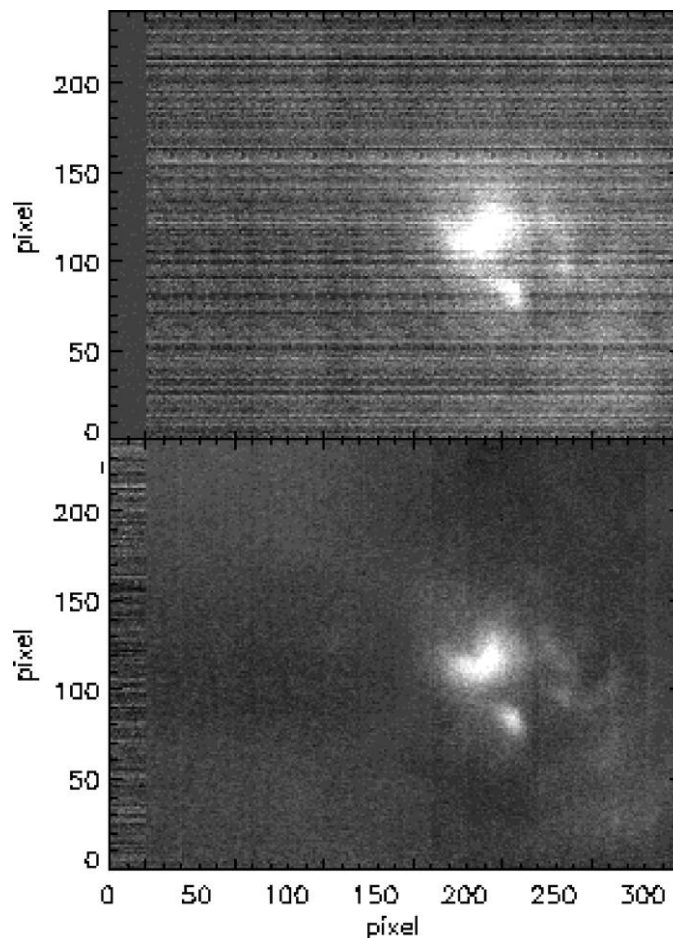

FIG. 7.—Images of the Trapezium in the Orion Nebula before and after the pattern noise was median filtered from the image. The images were acquired at 10 μm. East is to the left, and North is to the top of the image. The images are displayed on the same linear scale. The readout channel on the left side has been artificially set to zero in the top image. In the bottom image, the pattern noise has been reduced by median filtering. The channel pattern noise is reproduced in the leftmost channel of the bottom image.

headers contain target, telescope, observer, and exposure information that must be entered by the observer. The first step in processing the images is usually to subtract the chop and/or nod frames and produce a single image from the multiextension FITS file. Then the gain correction can be applied, and the pattern noise filtering performed, as described in previous sections.

Depending on the chop-nod strategy and throw used, the image contains one or more images of the source (with half of them negative); the individual images can be combined to improve S/N. When one has many of these frames taken at different offset positions, they can all be combined to produce a mosaic of the field. By observing a standard star at the same frame time, one can determine the Jy/ADU factor to apply to the image to calibrate the data.

For spectral data, one has a dispersed image with the spatial direction along the short dimension of the array and wavelength in
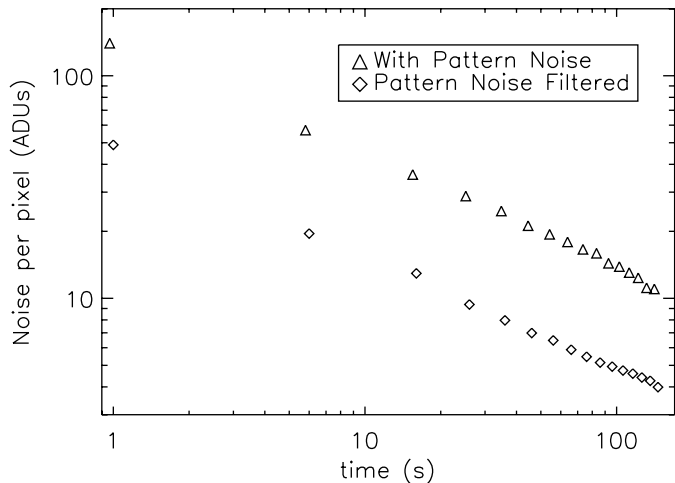
FIG. 8.—Noise per pixel as a function of integration time for MIRSI images with and without the pattern noise filtering.

the long direction. After the pattern removal and gain correction, spectral data-reduction tools such as the `twodspec` package in IRAF can then be used to define apertures and extract the spectra from the MIRSI images. The spectra are wavelength-calibrated using the data described in § 8.2. Using observations of standard stars at similar air mass and models of the stellar spectra, one can correct the spectra for instrumental and atmospheric transmission effects and produce flux-calibrated spectra of the targets.

The routines we developed to reduce pattern noise and perform other processing steps were written in IDL and are available from the authors at the MIRSI Web site.[4] Also available is an IDL reduction pipeline written by IRTF support astronomer E. Volquardsen.

7. IMAGING PERFORMANCE

The standard star observations used to measure the point-source sensitivities of MIRSI filters at the IRTF were acquired over the past few years. Most of the point-source sensitivities are measured from images of α Tau and β Peg acquired in 2002 November during commissioning. In 2004, μ UMa and β And were used to check the sensitivities at 8.7 and 11.6 μm. In 2006 July, images of α Lyr and γ Aql were used to check the sensitivity at 8.7 μm and measure the sensitivities at 12.3 and 24.5 μm.

7.1. Sensitivities

The standard stars were observed in such a way that the standard was located in only one of the four beam positions. After chop-nod subtraction, each image was flat-fielded by a gain map and the pattern noise removed as described above. The images

were averaged after registering to the peak location of the point source (identified by fitting a Gaussian to the standard PSF).

Fluxes from the standards at all observed wavelengths were measured from the images using aperture photometry. The measured fluxes were corrected for the observed air mass using extinction coefficients reported by Krisciunas et al. (1987). During commissioning, standards were observed at air masses of 1.5–1. For standards observed during 2004 and 2006, standards were observed at air masses less than 1.2.

Table 5 presents the sensitivities determined from the measured standard star flux for filters in MIRSI. Columns (1), (2), and (3) list the filter central wavelength, filter bandwidth, and the diffraction limit at the IRTF corresponding to the central wavelength. The flux ratios listed in column (5) are the ratios of the standard flux (Cohen et al. 1992, 1995) and the flux measured from images having exposure times listed in column (4). To determine the standard flux, we convolved the MIRSI filter curves with the Cohen spectral templates to calculate the standard star's flux specific to MIRSI filter set. The background noise per pixel (col. [6]) is the product of the flux ratios in column (5) and the standard deviation in the background measured in a 5.3″–8.0″ annulus. The reported noise is therefore specific to the exposure time provided in column four.

To calculate the sensitivities, we need to determine a reasonable aperture over which we would sample the flux from faint point sources. Because 99% of the total flux from a Gaussian PSF falls within a radius of 1.104 FWHM (Rice 1995), we assumed that the flux from a faint point source would fall within that radius. Figure 9 presents the radial profile and a processed image of α Tau at 11.6 μm. From a Gaussian fitted to the central core, the FWHM of the α Tau PSF is 0.89″, nearly diffraction-limited at 11.6 μm. Three diffraction rings are visible in the image and the magnified portion of the radial profile. At 10 μm, MIRSI should be diffraction-limited at the IRTF, and in our calculations, we used the diffraction limit as an estimate of a point-source FWHM.

Knowing the diffraction limit at the IRTF (Table 5 col. [3]), the number of pixels within a radius of 2.6 σ was calculated. If the diameter of the aperture calculated was less than three pixels, a 3-pixel diameter aperture was used (this occurs at 4 μm). The noise contributed by the background is then the product of the background noise per pixel and the square root of the aperture area in pixels.

The point-source sensitivities reported in column (7) of Table 5 are 1 σ measurements for a 1 minute on-source exposure. The projected 1 σ detection limit is calculated assuming that the noise diminishes with the square root of the exposure time. The projected sensitivities show that MIRSI can detect mJy sources in a few minutes. For diffuse emission, projected 1 σ sensitivities are reported in column (8) of Table 5. The sensitivities were determined in the same manner as the point-source sensitivities except that the aperture is over 1 arcsec^2.

---

[4] The MIRSI Web address is http://www.cfa.harvard.edu/mirsi/.

TABLE 5
SENSITIVITIES FOR DISCRETE FILTERS AND THE CVF

Wavelength (μm) (1)	Bandwidth (%) (2)	Diffraction limit at IRTF FWHM (arcsec) (3)	Exposure Time (s) (4)	Flux Ratio at IRTF (mJy/ADU) (5)	Background Noise (ADU) (6)	Point-source 1 σ detection at 1 min. (mJy) (7)	Diffuse-source 1 σ detection at 1 min. (mJy arcsec^{-2}) (8)
4.9	21	0.34	1.75	2.22	12.30	16.4	24.9
7.7	9.0	0.53	4.35	1.64	19.40	47.2	45.5
8.7	8.9	0.60	25.39	1.06	3.44	14.7	12.6
9.8	9.4	0.67	4.84	2.01	11.77	47.0	35.6
10.6	46	0.73	0.64	1.22	4.30	4.11	2.9
11.6	9.9	0.80	24.99	0.93	4.42	22.0	14.1
12.7	9.6	0.87	19.99	1.12	4.38	25.6	15.0
20.6	37	1.42	13.10	0.52	65.80	235.7	84.9
24.4	7.9	1.68	25.13	0.66	28.62	212.6	64.6
CVF	5						
10.2	5	0.72	21.8	5.8	2.19	53.8	40.6
10.6	5	0.76	21.8	4.6	2.21	43.1	32.5
11.6	5	0.83	21.8	4.8	2.21	44.3	32.5
12.6	5	0.89	21.8	5.5	2.51	58.6	45.0

7.2. CVF Wavelength Calibration

The initial function for positioning the CVF to the desired wavelength was based on the wavelength range of the CVF as specified by the manufacturer and the physical position of the CVF in the filter wheel. This calibration has recently been shown to be off by approximately 0.5 μm. This offset is large enough that if an observer tried to isolate emission for a particular line such as [S IV] at 10.5, the image probably did not properly sample the desired region of the spectrum.

In 2008 June we performed additional CVF calibration measurements. With the instrument mounted on the telescope, we observed the back of a warm aluminum window cover using the CVF in combination with three filters: 8.6, 9.8, and 11.6 μm. For each filter, the CVF was stepped in units of 0.1 μm across the filter bandpass and the spectral energy distribution (SED) was measured. For each filter, we compared the SED of the window cover as measured through the three filters to the transmission curves for the filters measured at 5 K. Because the CVF has a 5% bandpass, the observed flux as a function of wavelength is effectively smoothed by the filter transmission curve. A shift and scale change in the number of raw motor steps per micron was needed to center the observed SEDs on their corresponding filter transmission curves.

The new formula for positioning the CVF is motor position $= (13.675 - \lambda) \times 1223 + 9000$ where λ is in units of microns. The new calibration will be applied to the software for the IRTF 2008B observing semester. This means that the central wavelength for all CVF data taken prior to the 2008B observing semester should be shifted. The amount to shift the central wavelength is: $\lambda_{\mathrm{new}} = 0.97 \times \lambda_{\mathrm{old}} - 0.03$ μm, where both the new and old wavelengths are in units of microns.

FIG. 9.—Radial profile of α Tau at 11.6 μm. The dashed line is a Gaussian fit to the profile, and the solid line represents a Gaussian with a FWHM equal to the diffraction limit at 11.6 μm. The wing of the same profile is plotted at the bottom of the graph after being magnified by 100. In the upper right, an image of α Tau is plotted on a log scale to show the diffraction rings.

8. SPECTROSCOPIC PERFORMANCE

8.1. Sensitivity

The 10 μm grism sensitivities were determined from observations of α Tau. Five grism spectra of α Tau with maximum flux values greater than 1000 counts were co-added, and the spectrum was extracted from the co-added image using the `apall` routine in IRAF. We determined the ADU-to-Jy ratio by dividing the extracted spectrum by the standard flux for α Tau (Cohen et al. 1995). Next, the co-added image was divided by the ADU/Jy. The uncertainty in the background from 8–13 μm was determined by calculating the standard deviation

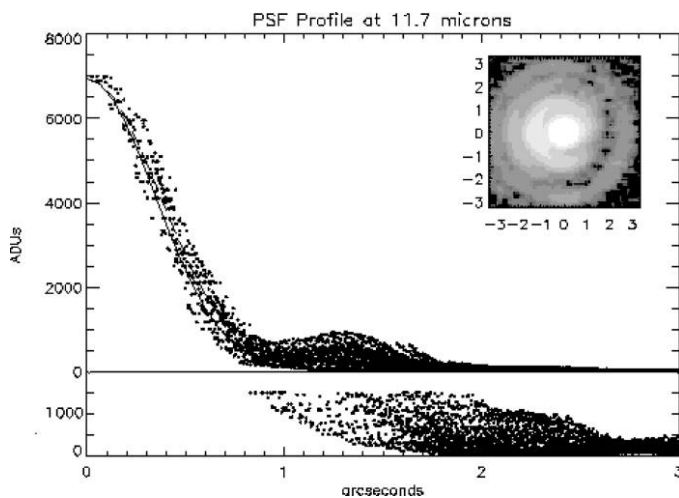in 41 pixels below the α Tau spectrum in the co-added spectrum. Above the spectrum, the sensitivity is worse because of channel offsets that are common when a bright source is detected (see § 5). The total on-source time for the co-added spectrum is 43.5 s. The sensitivity at 1 minute was calculated by assuming the noise is inversely proportional to the square root of the exposure time.

Figure 10 shows the 8–13 μm grism sensitivity. At 10 μm, the sensitivity is 75 mJy for 1 minute of on-source integration time. The sensitivities plotted in Figure 10 include the effects of the 10 μm broad band filter. The transmission curve of the 10 μm filter prevents the detection of 13–14 μm radiation.

8.2. Wavelength Calibrations

8.2.1. 10 μm Grism

We determined the calibration of the 10 μm grism using spectra of the Orion Bar acquired at the IRTF (Kassis et al. 2006). The mid-infrared spectrum of the Orion bar exhibits emission from ionized gas, warm dust, and polycyclic aromatic hydrocarbons (Kassis et al. 2006). Lines of [Ar III], [S IV], and [Ne II] in the spectrum of the Orion Bar are assumed to be emitting at 8.99, 10.51, and 12.81 μm, respectively (Glass 1999 and references therein). Kassis et al. (2006) used the wide slit ($R \sim 100$) while acquiring spectra of emission from the Orion Bar in chop-nod mode.

A Gaussian of width 3.76 pixels adequately fit the ionized gas line profiles. The pixel locations of the best fitted Gaussian to the line profiles were 55.17, 137.61, and 260.12 for [Ar III], [S IV], and [Ne II], respectively. A linear fit to the line wavelength and peak position result in a spectral coverage of 7.955–13.926 μm, and a pixel dispersion of 0.01866 μm pixel^{-1}. This results in an R of 113.9 at 7.955 μm and 198.5 at 13.926 μm using the wide slit. The accuracy of the calibration is estimated to be ± 0.01 μm.
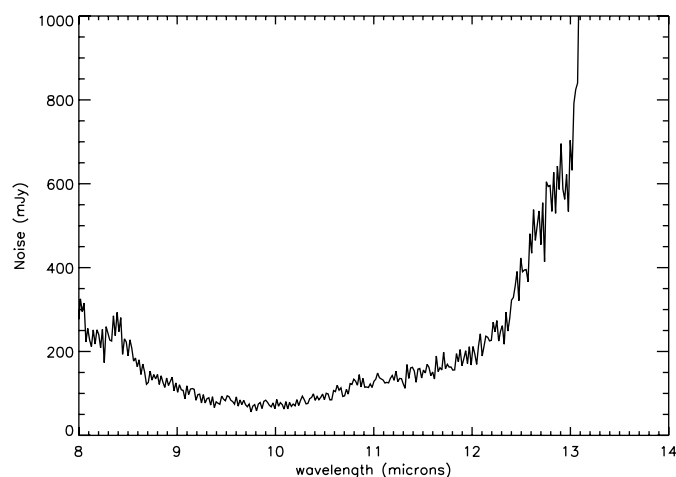

FIG. 10.—Grism sensitivity at 8–13 μm as determined from observations of α Tau. The 1 σ sensitivities correspond to 1 minute of on-source integration time.

We also observed the planetary nebula NGC 7027 in 2002 November using the narrow slit in order to calibrate the wavelength scale in the higher resolution mode. The same three lines of [Ar III], [S IV], and [Ne II] were detected and used for the calibration. A linear fit to the wavelength scale gave a value of 0.01910 μm pixel^{-1}, starting at 7.9381 μm. The resolution at 10.52 μm was measured to be $R = 202$.

8.2.2. 20 μm Grism

An initial test and calibration of the 20 μm grism was performed in the lab at Boston University before the instrument was delivered to the IRTF. A hot blackbody source was positioned in front of the instrument aperture. The grism was used in conjunction with the 17–25 μm filters to measure the transmission through several of the bandpasses, and the filter manufacturer's transmission curves were compared to the data to determine the wavelength at various pixel locations and thus to derive the wavelength calibration of the grism. The calibration was consistent with what was expected from the optical design. However, the filter curves used were from room temperature measurements, so the calibration was expected to be slightly off due to the wavelength shifts in the transmission of the filters at 4 K.

We later performed a calibration of the grism based on observations obtained at the IRTF in 2008 June. Spectral images were obtained in chop mode with the wide slit of the star α Her (Fig. 11). The spectra were extracted using an aperture file from a 10 μm standard star observation as a reference. The extracted spectrum is shown in Figure 11. The shape is determined by the grism throughput, the stellar spectrum, and the atmospheric absorption. We compared this observation to the ATRAN model of the atmospheric absorption for Mauna Kea convolved to a resolution of 100, made with K. Volk's Web page calculator.[5] The measured spectrum was matched to the ATRAN model plot to determine a linear pixel dispersion of 0.0325 μm pixel^{-1}, with the first pixel at 16.9195. Again, the accuracy of the calibration is estimated to be ± 0.01 μm.

We consider the later calibration of the 20 μm grism to be more accurate than the earlier lab results due to the reasons noted above, rather than measuring any real change in the instrument. The wavelength calibration of both grisms should be stable over time because it depends on the relative positions of the array and optical elements, which have not been disturbed since the instrument was delivered to the IRTF. Therefore, the more recent calibration should be used for all 20 μm grism observations, and should replace the lab calibration for any data taken prior to 2008 June, as well as afterward.
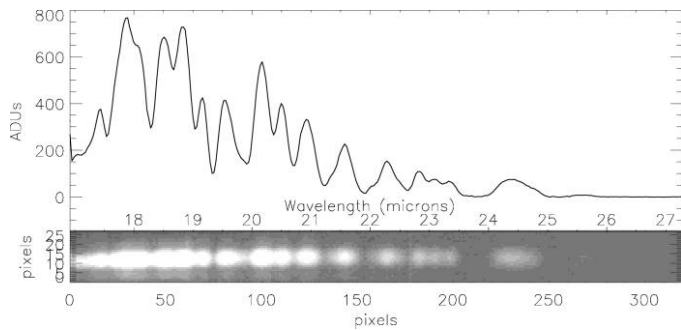
_____

[5] This calculator can be accessed at http://staff.gemini.edu/~kvolk/trans.html.

Fig. 11.—α Her 20 μm spectra obtained with MIRSI. The plot shows the extracted spectrum and the raw spectrum of the standard in the MIRSI image. The data have not been corrected for instrumental or atmospheric transmission effects.

9. MIRSI IN THE *SPITZER* ERA

MIRSI is located at one of the best ground-based sites for IR observing, but it cannot match the sensitivity of the *Spitzer Space Telescope* IRAC and MIPS instruments, which can detect sources in the μJy range in a matter of minutes. However, MIRSI is complementary to IRAC and MIPS in several ways. First, MIRSI has over a factor of 3 better spatial resolution, due to the larger IRTF primary mirror. MIRSI can therefore be used to resolve compact sources and separate multiple components that are detected with IRAC and MIPS. MIRSI also has many narrowband filters and grism spectroscopy modes, allowing sources to be better characterized than is possible with the broad filters used by the *Spitzer* instruments.

The *Spitzer* instruments were optimized for the study of faint sources under low background conditions, which makes them not well suited for observing bright sources. For example, in the shortest full-array frame time, sources brighter than 3 Jy will saturate the 8 μm channel. Therefore IRAC cannot be used to study Jupiter or Saturn effectively, for example, or many of the sources detected by IRAS. MIRSI can quickly detect sources in the >0.1 Jy range, so it can be used for sources that are difficult to observe with IRAC.

Spitzer's cryogen supply is expected to be exhausted sometime in 2009 April, and the last proposal cycle has already occurred. Therefore, no new projects are possible, outside of Director's Discretionary Time proposals. Any new findings or discoveries in the *Spitzer* data will have to be followed up at other facilities. After the cryogens are expended, it is anticipated that the 3.6 and 4.5 μm bands of IRAC will continue to operate at their nominal sensitivity. It is expected that there will be an extended *Spitzer* mission lasting as long as until 2014 that will use these two bands. MIRSI can be used for follow-up observations of sources that are detected in the surveys that will be conducted in the warm mission, when no other longer wavelength capability will exist on *Spitzer*. SOFIA will be just starting to conduct science operations during this time, and the James Webb telescope will be several years away from launch. Therefore, MIRSI and the other ground-based mid-IR instruments will continue to fulfill a useful function in terms of resolution and wavelength coverage for several years to come.

REFERENCES

Baines, K. H., et al. 2007, Science, 318, 226

Campbell, M. F., et al.. 2008, ApJ, 673, 954

Cohen, M., Walker, R. G., & Witteborn, F. C. 1992, AJ, 104, 2030

Cohen, M., Witteborn, F. C., Walker, R. G., Bregman, J. D., & Wooden, D. H. 1995, AJ, 110, 275

Deutsch, L. K., Hora, J. L., Adams, J. D., & Kassis, M. 2003, Proc. SPIE, 4841, 106

Estrada, A. D., et al. 1998, Proc. SPIE, 3354, 99

Fernandez, Y. R., Lisse, C. M., Schleicher, D. G., Bus, S. J., Kassis, M., Hora, J. L., & Deutsch, L. K. 2004, BAAS-DPS, 36, 1117

Glass, I. S. 1999 Handbook of Infrared Astronomy (Cambridge, UK: Cambridge University Press)

Harker, D. E., Woodward, C. E., Wooden, D. H., & Kelley, M. S.. 2004, BAAS, 205.5612

Hoffmann, W. F., Fazio, G. G., Shivanandan, K., Hora, J. L., & Deutsch, L. K. 1993, in Infrared Detectors and Instrumentation, ed. A. M. Fowler, Proc. SPIE 1946, 449

Hoffmann, W. F., Hora, J. L., Fazio, G. G., Deutsch, L. K., & Dayal, A. 1998, in Infrared Astronomical Instrumentation, ed. Fowler, A., Proc. SPIE 3354, 647

Kassis, M., Adams, J. D., Campbell, M. F., Deutsch, L. K., Jackson, J. M., & Tollestrup, E. V. 2006, ApJ, 637, 823

Krisciunas, K., et al. 1987, PASP, 99, 887

Mueller, M., Harris, A. W., Bus, S. J., Hora, J. L., Kassis, M., & Adams, J. D. 2006, A&A, 447, 1153

Raytheon: Astronomy Team 1999, User's Guide and Operating Manual, CRC-774 320x240 Readout Integrated Circuit

Rice, J. A. 1995, Mathematical Statistics and Data Analysis (Belmont, Calif: Wadsworth Publishing Company)

Sako, S., et al. 2003, PASP, 115, 1407

Sánchez-Lavega, A., et al. 2008, Nature, 451, 437

Smith, N., Bally, J., Shuping, R. Y., Morris, M., & Kassis, M. 2005, AJ, 130, 1763

Tedesco, E. F., Bottke, W. F., Bus, S. J., Volquardsen, E., Cellino, A., Delbo, M., Davis, D. R., Morbidelli, A., Hora, J. L., Adams, J. D., & Kassis, M. 2005, BAAS-DPS, 643

APPENDIX

IRAF DISTORTION DATABASE FILE FOR MIRSI

TABLE 6

IRAF Distortion Database File Output Produced by
the IRAF Function Geomap Using a Second-order
Polynomial Fit to the Offset Data Positions

begin	griddata_rev0.txt	
xrefmean	158.965	
yrefmean	120.0264	
xmean	−0.1388889	
ymean	0.1853884	
geometry	general	
function	polynomial	
xshift	42.6572	
yshift	31.90394	
xmag	0.2689426	
ymag	0.2635491	
xrotation	179.8851	
yrotation	180.0792	
xrms	0.1575143	
yrms	0.1697925	
surface1	11	
	3.	3.
	2.	2.
	2.	2.
	0.	0.
	−310.	−310.
	310.	310.
	−250.	−250.
	250.	250.
	42.6572	31.90394
	−0.268942	−5.393603E−4
	−3.643442E−4	−0.2635489
surface2	17	
	3.	3.
	3.	3.
	3.	3.
	1.	1.
	−310.	−310.
	310.	310.
	−250.	−250.
	250.	250.
	0.009234399	0.06443879
	−2.025740E−4	0.002863407
	3.937325E−7	−1.394265E−5
	0.003527451	−0.001944497
	−3.185834E−5	−1.234190E−5
	5.410980E−8	7.550739E−8
	−2.031161E−5	4.720995E−6
	1.648216E−7	4.327962E−9
	−2.091021E−10	1.504998E−11